

Curtis K. Stimpson¹

Mem. ASME
Department of Mechanical
and Nuclear Engineering,
The Pennsylvania State University,
3127 Research Drive,
State College, PA 16801
e-mail: curtis.stimpson@psu.edu

Jacob C. Snyder

Mem. ASME
Department of Mechanical
and Nuclear Engineering,
The Pennsylvania State University,
3127 Research Drive,
State College, PA 16801
e-mail: jacob.snyder@psu.edu

Karen A. Thole

Mem. ASME
Department of Mechanical
and Nuclear Engineering,
The Pennsylvania State University,
136 Reber Building,
University Park, PA 16802
e-mail: kthole@psu.edu

Dominic Mongillo

Pratt & Whitney,
400 Main Street,
East Hartford, CT 06118
e-mail: dominic.mongillo@pw.utc.com

Scaling Roughness Effects on Pressure Loss and Heat Transfer of Additively Manufactured Channels

Additive manufacturing (AM) with metal powder has made possible the fabrication of gas turbine components with small and complex flow paths that cannot be achieved with any other manufacturing technology presently available. The increased design space of AM allows turbine designers to develop advanced cooling schemes in high-temperature components to increase cooling efficiency. Inherent in AM with metals is the large surface roughness that cannot be removed from small internal geometries. Such roughness has been shown in previous studies to significantly augment pressure loss and heat transfer of small channels. However, the roughness on these channels or other surfaces made from AM with metal powder has not been thoroughly characterized for scaling pressure loss and heat transfer data. This study examines the roughness of the surfaces of channels of various hydraulic length scales made with direct metal laser sintering (DMLS). Statistical roughness parameters are presented along with other parameters that others have found to correlate with flow and heat transfer. The pressure loss and heat transfer previously reported for the DMLS channels studied in this work are compared to the physical roughness measurements. Results show that the relative arithmetic mean roughness correlates well with the relative equivalent sand grain roughness. A correlation is presented to predict the Nusselt number of flow through AM channels, which gives better predictions of heat transfer than correlations currently available. [DOI: 10.1115/1.4034555]

Introduction

The capabilities and advantages of additive manufacturing (AM) are being explored in nearly every industry in hopes of developing products that have improved functionality, efficiency, and cost; the gas turbine industry is no exception. Leading manufacturers of gas turbine engines have already begun fabricating production parts with AM [1]. These companies primarily employ methods of AM that build metal components using selective laser sintering, selective laser melting, electron beam melting, or direct metal laser sintering (DMLS). These methods are able to produce parts from high-temperature alloys in shapes that cannot otherwise be produced. Other advantages of these techniques are decreased production cost, material/weight reduction, and greater design freedom.

As with any manufacturing process, it is crucial to understand the limitations of AM. One limitation with metal parts produced with AM is that they typically do not have the same mechanical properties as do wrought or cast parts of the same material. A common misconception about additive processes is that one can make any shape with them. Even though there is more design freedom, there are significant limitations as to what features can be built and in what orientations they can be built. A designer must be aware of these limitations early in the design process if the advantages of AM are to be properly leveraged.

A natural consequence of the metal AM processes listed above is the relatively rough surface finish that results from the metal particles sintering to the surfaces of the part during fabrication. These roughness levels have significant effects on the pressure loss and heat transfer of parts with internal flow channels [2,3]. The effects of roughness must be accounted for in the design stage. The authors of this paper previously presented flow and heat transfer measurements that show the effects of roughness [2]. This previous study did not investigate how or why the roughness was affecting the flow in the way it was. The current work attempts to answer those questions by presenting more detailed roughness characterization and analytical tools for predicting the flow and heat transfer through microchannels made with AM.

Review of Literature

Roughness effects on flow friction have been studied for many decades. Nikuradse's pioneering work on flow through tubes roughened with sand grains formed the basis for how roughness is currently treated for internal flows [4]. He defined relative roughness, k_s/d , where k_s is the diameter of the sand grains adhered to the walls of a pipe of diameter, d . This parameter was adopted by many in their work, including Moody whose diagram of friction factor versus Reynolds number for various values of k_s/d can be found in nearly every introductory fluid mechanics book published in recent decades [5]. Because this parameter was not formed using measurements of the resulting pipe wall surface roughness, correlations based on this parameter are hardly useful for predicting flow friction when physical roughness measurements are the only data available. One must obtain k_s/d

¹Corresponding author.

Contributed by the International Gas Turbine Institute (IGTI) of ASME for publication in the JOURNAL OF TURBOMACHINERY. Manuscript received July 21, 2016; final manuscript received August 8, 2016; published online September 27, 2016. Editor: Kenneth Hall.

Table 1 Coupon design specifications and parameters measured with CT scanning

Coupon name	Material	Number of channels	Design width (μm)	Design height (μm)	Design D_h (μm)	Design S/D_h	Measured width (μm)	Measured height (μm)	Measured D_h (μm)	R_a (μm)	R_a/D_h
L-1x-Co	CoCr	24	457	1016	631	1.33	450	1028	626	9.6	0.015
L-2x-Co	CoCr	16	914	2032	1261	1.03	898	2036	1246	12.3	0.010
M-1x-Co	CoCr	24	305	660	406	2.06	296	694	415	10.3	0.025
M-2x-Co	CoCr	16	610	1321	834	1.55	516	1302	739	12.7	0.017
S-2x-Co	CoCr	16	610	610	610	2.12	601	626	614	9.5	0.015
L-1x-In	Inco 718	24	457	1016	631	1.33	453	1047	632	10.5	0.017
L-2x-In	Inco 718	16	914	2032	1261	1.03	919	2083	1275	10.9	0.009
M-1x-In	Inco 718	24	305	660	406	2.06	355	690	469	11.9	0.025
M-2x-In	Inco 718	16	610	1321	834	1.55	683	1406	920	13.8	0.015
S-2x-In	Inco 718	16	610	610	610	2.12	660	669	664	13.3	0.020

experimentally, which is why the roughness scale k_s is commonly referred to as the equivalent sand grain roughness and is not representative of a physical roughness measurement [6].

Many have worked to correlate k_s with a physical roughness measurement including early work done by Schlichting [7] who measured k_s for different artificial roughness elements arranged in various arrays. More recent efforts of many others studying external flow over rough surfaces were reported by Bons [8]. The literature regarding flow over rough surfaces seems to be dominated by external flow configurations of which several use artificially roughened surfaces instead of random roughness. There are studies that have examined internal flow through randomly roughened channels. Weaver et al. [9] studied micro-channel flow with rough surfaces; however, these surfaces were roughened with electrical discharge machining which resulted in smaller roughness than the DMLS process. Huang et al. [10] expanded on the work performed by Nikuradse [4] examining roughened tubes with relatively large sand grains where k_s/d was between 0.21 and 0.42. These are much more comparable to what was reported previously by the current authors [2], but physical roughness measurements were not reported in the work of Huang et al. [10]. In recent years, work has been done to characterize flow through microchannels with large relative roughness. Brackbill and Kandlikar [11] studied flow through channels with large relative roughness and presented a useful literature review on work that has been done regarding rough flow through microchannels and nanochannels. However, due to the small length scales of the channels, most data reported in the literature are for low Reynolds number flows ($Re < 2300$); little data exist in the literature for the turbulent regime, which is of most interest in this study.

Heat transfer correlations for turbulent flow through very rough channels are equally difficult to find. Morini [12] gives a thorough literature review of heat transfer studies of flow through microchannels. This shows that very little has been done to characterize heat transfer through channels similar to those studied by the current authors.

The uniqueness of this work is that it examines the friction and heat transfer results of turbulent flow through very rough microchannels made with DMLS and that it presents predictive correlations using physical surface roughness measurements. To the authors' knowledge, comparable work has not yet been published in open literature.

Methods

To better understand how roughness impacts the pressure loss and heat transfer in DMLS microchannels, it is necessary to collect detailed topographical data from the channel surfaces. Therefore, the data were collected using a few different approaches in hopes to identify one or more key parameters that correlate with the flow and heat transfer performance. This section discusses the test specimens that were used for this study, the

methods used to collect surface roughness data, and how the roughness data were reduced into roughness parameters that are commonly found in the literature.

Description of Test Coupons. The coupons used in this study are the same as those used in the authors' previous study [2]. Ten coupons were investigated, all of which were made with DMLS; details on the coupons can be found in Table 1. Five of the coupons were made using cobalt-chrome-molybdenum-based superalloy (CoCr) powder [13] with each having a unique channel width and height combination. The remaining five were made from an Inconel™ 718 (Inco) powder [14] and nominally had the same geometry as the five made from CoCr. All ten coupons were 25.4 mm in length and in width.

Each coupon was built at a 45 deg angle from the horizontal as shown in Fig. 1 using material-specific build parameters calculated according to the recommendations of the DMLS machine manufacturer [15]. Snyder et al. [3] showed that a 45 deg build direction results in higher friction drag than a vertical build direction for round channels. This is due to the large roughness on downward-facing surfaces that exists at every build orientation except vertical; vertically oriented surfaces are much smoother. Building all flow channels in a vertical orientation would seem like a simple method to minimize friction loss in a design, but it is highly unlikely that a working design of a gas turbine component would contain channels that are to be built only in the vertical direction. Therefore, a 45 deg build direction was used in this study to capture the combined effects of downward-facing, upward-facing, and vertical surfaces. In a working design, the build orientation could be used as a method to control flow rates and tune convective heat transfer coefficients.

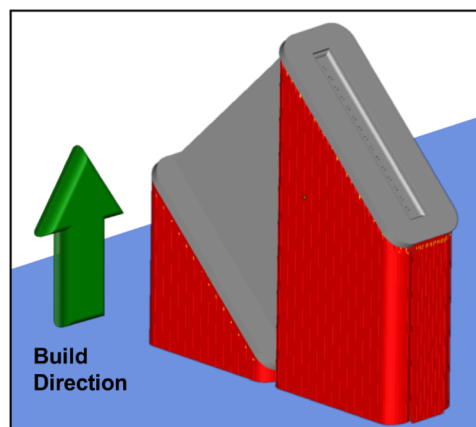


Fig. 1 Build orientation and support structures of the DMLS coupons

The CoCr and the Inco powder particles used for fabrication were spherical in shape and were sieved to obtain an average particle size of $30\ \mu\text{m}$. The height of each build layer during fabrication was $40\ \mu\text{m}$. Further information about the coupon build process including details on machine parameters, support structures, heat treating, and other post processing is given by Snyder et al. [3].

Channel Dimensions and Roughness Measurements. Industrial computed tomography (CT) scanning was used in the authors' previous study [2] to characterize the internal channel dimensions. CT scanning was selected because it is a nondestructive inspection technique that generates a three-dimensional reconstruction of the entire part. CT scanning each part enabled accurate measurements of internal channel dimensions without cutting the coupons open to expose the channel surfaces, thereby permanently destroying the coupons. An important geometric scale necessary for flow and heat transfer data reduction, namely, hydraulic diameter, D_h , was derived from these measurements. Findings indicated that the design intent was not met for each of the channels using the DMLS process, and for this reason, part dimensions were determined using the CT data. D_h and other geometric parameters are given in Table 1. All values in Table 1 represent the average over every channel in each coupon.

The CT scanning instrument was capable of resolving roughness features as small as $30\ \mu\text{m}$. This ability can be seen in the small surface sample given in Fig. 2(a), which shows the ability of the CT scanning method to resolve the larger roughness features. Because many roughness features were larger than the resolution of the machine, it was possible to obtain semiquantitative roughness estimates for surfaces using the CT scans. A description of how this was done can be found in the authors' previous paper [2]. Surface roughness results from that study are shown in Table 1 where the uncertainty of R_a is estimated to be about $\pm 4\ \mu\text{m}$. Again, these values represent an average over all channels in each coupon.

In addition to CT scanning, two other methods were used to characterize the roughness of the channel: white light interferometry and scanning electron microscopy. Data from all three methods were used because each technique adds unique information about the surface morphology.

A scanning white light interferometer, also known as an optical profilometer (OP), was used to detect the height of discrete points on a sample surface. Surface data collected with the OP are shown in Fig. 2(b) compared to the CT scan rendering of the same surface (Fig. 2(a)). A few coupons were prepared for analysis with the OP by cutting them open to expose the inner faces of the channel. The OP collected data for each surface by scanning it in the direction normal to that surface while illuminating it with light. As a scan proceeded, a camera would detect interference patterns reflecting off of the surface and record the height at the specific location of those patterns. This generated a three-dimensional

point cloud with a resolution in the plane of the surface of 1024×1024 pixels. The magnification used for collecting the data presented here resulted in a lateral resolution of $1.64\ \mu\text{m}$ and a resolution $\ll 1\ \mu\text{m}$ in the direction normal to the surface.

Preparing samples from all channel surfaces and measuring them all with an OP was prohibitively difficult and time consuming for the scope of this study. Therefore, only a select few surface specimens were prepared and analyzed with the OP. These specimens came from four different coupons: two from the group of CoCr coupons and two from the Inco. No statistical difference in roughness between different coupons from the same material was found. This is corroborated by the CT scan data presented previously by the authors [2].

Although an OP is capable of very fine resolution, there are some limitations to this technique. Because the OP uses a camera placed above the sample, it can only register points on the surface that it can view; regions overshadowed by overhanging features will not be captured. For example, if a sphere is being scanned, only the upper hemisphere will be visible by the camera. The OP can resolve the curvature of the upper hemisphere, but it is not possible to collect any data from the lower hemisphere as it cannot be seen by the camera. Another shortcoming of this technique is that it has poor resolution of steep gradients due to the sharp viewing angle of the camera relative to the surface. These shortcomings result in scans that show great detail on surfaces that are visible to the camera and little or no information about very sharp roughness features and overhanging features. OP data from surfaces with these types of features may poorly represent the actual surface morphology. However, there is not a reasonable alternative known by the authors that can measure these highly three-dimensional surfaces with the accuracy of an OP.

Once the point cloud data were obtained from the OP, it was tessellated without significant modifications to the data points. Due to the limitations of the measurement method just discussed, very rough surfaces would often have many holes in the mesh. These holes were patched using an algorithm that interpolated the points around the hole to infer the surface shape. Most of the holes were found in regions where the surface was either vertical or undercut; repairs in these areas were not expected to be a very good match of the actual surface structure. After filling the holes, the mesh was further repaired by flipping elements that were oriented incorrectly and by fixing other mesh errors. Next, the mesh was decimated to reduce the number of nodes in the mesh using algorithms that preserved the surface topology. Finally, the surface was altered to remove any waviness that might result in a bias of the roughness analyses by using a low-order polynomial fit. The surface mesh was then prepared for roughness parameter calculations using the methods described the Roughness Quantification section. The sample surface rendering of the OP data given in Fig. 2(b) compared to the rendering of the CT data for the same surface location exhibits the superiority of using data from an OP for quantitative roughness analysis over using data from a CT scan.

The third surface characterization approach used a scanning electron microscope (SEM) to collect micrographs of the surface like the one shown in Fig. 3(a). Although SEM micrographs are not particularly useful for providing quantitative roughness results, they are extremely useful for qualitatively representing the topology of the surface with high resolution. The method with which an image is generated using an SEM results in shadowing that brings out the complex three-dimensional morphology of a surface. Despite an SEM collecting merely a two-dimensional image, indications of overhanging surfaces and contours are made visible where it would be impossible to see them with an OP. Additionally, an SEM is capable of collecting images showing features much smaller than $1\ \mu\text{m}$ with good resolution. The micrograph shown in Fig. 3(a) is placed next to a rendering of OP data collected from the same location. One can see that the OP is picking up nearly all the features on the surface although it does not show quite as much detail as the SEM image. However, the

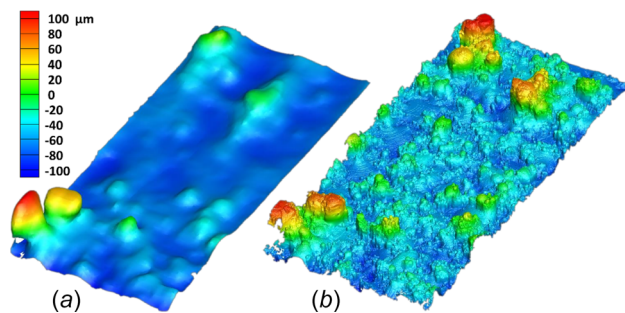


Fig. 2 Comparison of (a) CT scan reconstruction and (b) surface rendering from optical profilometer data of the same location on a downward-facing surface of a CoCr coupon

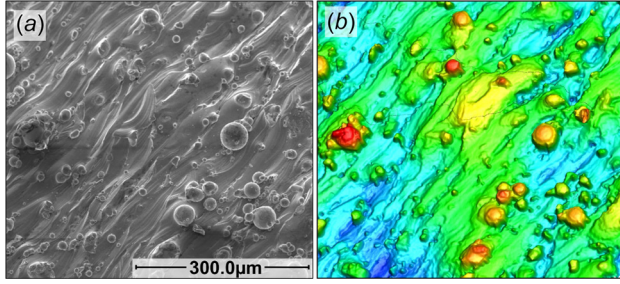


Fig. 3 Comparison of (a) SEM micrographs and (b) surface rendering from optical profilometer data of the same location on a vertical surface of a CoCr coupon

spherical roughness elements in the SEM micrograph do not appear spherical in the OP rendering as might be expected considering the limitations of the OP.

Roughness Quantification. Only the OP data were used for quantitative roughness analysis. It was analyzed using three different approaches in attempt to find the best method of correlating the physical roughness measurements to the effect that the roughness had on the pressure loss and heat transfer in the coupons. The first method was a basic statistical approach that involved the calculation of five roughness parameters: arithmetic mean roughness, R_a , root-mean-square (RMS) roughness, R_q , mean roughness depth, R_z , skewness, R_{sk} , and kurtosis, R_{ku} . The mathematical definitions of each are given in Eqs. (1)–(5), respectively. Figure 4 gives graphical definitions of roughness height for a given point, z_i , the mean surface height, μ , the highest point for a given region, z_{max} , and the lowest point for a region, z_{min} , for a two-dimensional slice of a sample surface. Note that the statistical roughness parameters were calculated from the three-dimensional data rather than a slice of the data as illustrated in Fig. 4.

$$R_a = \frac{1}{n} \sum_{i=1}^n |z_i - \mu| \quad (1)$$

$$R_q = \sqrt{\frac{1}{n} \sum_{i=1}^n (z_i - \mu)^2} \quad (2)$$

$$R_z = \frac{1}{5} \sum_{i=1}^5 (z_{max} - z_{min})_i \quad (3)$$

$$R_{sk} = \frac{1}{nR_q^3} \sum_{i=1}^n (z_i - \mu)^3 \quad (4)$$

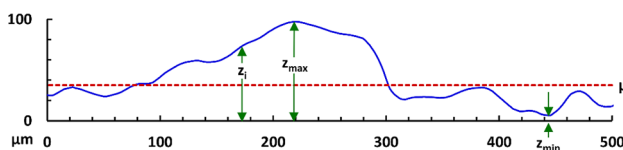


Fig. 4 Sample of roughness slice from optical profilometer data (axis scales are equal)

$$R_{ku} = \frac{1}{nR_q^4} \sum_{i=1}^n (z_i - \mu)^4 \quad (5)$$

Each statistical roughness parameter gives unique information about a surface. The arithmetic mean roughness, R_a , represents the average deviation of each point from the mean and is easy to understand given the definition in Eq. (1). Similarly, Eq. (2) gives a straightforward definition of the RMS roughness, R_q . The mean roughness depth, R_z , can be defined in various ways. Here, it is defined as the average of the highest minus the lowest point for five different regions as shown in Eq. (3). Computing this value from the OP data involved dividing each dataset into five equal regions, computing the height difference between the highest and lowest points of each region, and finally averaging the five values. This represents the prominence of the largest features on average. The skewness, R_{sk} , is a measure of how the data are distributed about the mean. A positive skewness indicates that there are more positive, peaklike features, and a negative skewness indicates that there are more negative, valleylike features. The last statistical parameter is the kurtosis, R_{ku} , and is a measure of the width of the distribution relative to a Gaussian distribution. A large kurtosis here would imply that the surface profile changes dramatically and has sharp peaks; a small kurtosis suggests a smoother change in roughness or large plateaus instead of peaks.

The second approach used for analyzing the roughness data obtained with the OP involved calculating the correlation length for the surfaces. This was done by first taking several slices of each surface in the direction of flow. The autocorrelation function (ACF) was then solved for various lengths, L , on each slice. The ACF is represented mathematically as

$$ACF = \frac{1}{nR_q^2} \sum_{i=1}^n (z_i - \mu)(z_{i+m} - \mu) \quad (6)$$

where n is the number of data points on the slice and m is the number of points contained in the specified length, L . This ACF returns a value that indicates how well the slice correlates with itself for a given L . A value of unity means that the profile correlates perfectly, and a value of zero suggests that it is completely uncorrelated. Random datasets are likely to have some length at which $ACF=0$; however, because of the random nature of real surfaces, it is also possible that the $ACF > 0$ for all possible lengths, L . Therefore, it is necessary to select a specific ACF value for which the surface is no longer considered to correlate. The value 0.2 was selected here as it seemed reasonable and has been used by others [16]. The minimum distance for which the ACF is always greater than 0.2 for all slices of a given surface is known as the correlation length, λ .

Figure 5 shows the ACF plotted at various lengths, L , for slices of a downward-facing surface of CoCr coupon; λ is also illustrated in the figure. This method can be useful for determining dominant length scales of the roughness as well as periodic patterns if they exist. A dominant length scale would give a similar ACF profile for all slices while $ACF > 0.2$, and periodic patterns would show up as an oscillation of the ACF about $ACF=0$ with discernable periods.

A third analysis method was used in attempt to corroborate or build upon the multitude of studies mentioned previously that have successfully made use of a combined roughness density and shape factor, Λ , first introduced by Dirling [17] to correlate drag and heat transfer. Because the roughness of the DMLS surfaces is random in nature, the definition of this parameter given by van Rij et al. [18] seems most appropriate here. This is given by

$$\Lambda = \left(\frac{A}{A_f}\right) \left(\frac{A_f}{A_w}\right)^{-1.6} \quad (7)$$

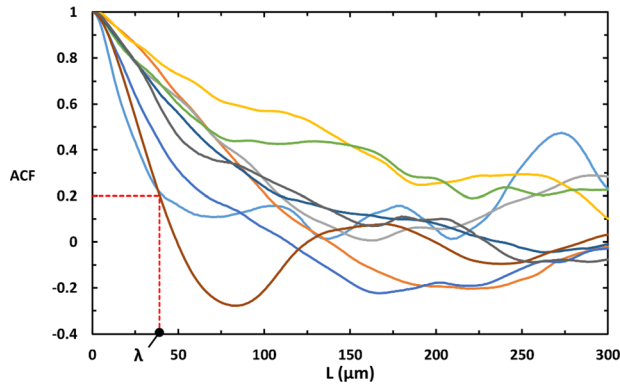


Fig. 5 Autocorrelation plotted versus offset length for several slices along a simple surface; λ indicates the correlation length

where A is the flat reference area (i.e., area of a flat surface without roughness), A_f is the total frontal area relative to the flow direction, and A_w is the total windward wetted area. These three different areas were calculated using the mesh file generated from each OP dataset. The calculation of A was trivial. A_f was calculated by taking the dot product of each face normal vector with the negative of the flow direction vector and summing the resulting values that were greater than zero. A_w was calculated by summing the total area of all mesh elements that resulted in a positive value when their normal vector was dotted with the negative of the flow direction vector.

Scaling Results

The results of the scaling analyses are presented in two sections. The first presents qualitative and quantitative

characterization of the channel surfaces. These characterization results are used to develop correlations to predict flow friction and heat transfer through AM channels with large roughness, which is the topic of the second section.

Surface Roughness. Results from the SEM micrographs will be discussed first as these provide qualitative information that will add to the discussion of the quantitative results. Figure 6 shows micrographs of all surface orientations for both alloys. A few key observations can be made from these images. First, individual roughness features on all surfaces look very much like the spherical-shaped powder used to fabricate the coupons. The diameter of these features is around $30\ \mu\text{m}$ suggesting that much of the roughness comes from powder particles being sintered or partially melted to the surface. Second, the surfaces of the CoCr coupons (Figs. 6(d)–6(f)) have many more spherical features than the surfaces of the Inco coupons (Figs. 6(a)–6(c)) suggesting that the CoCr powder had a greater propensity to sinter to the surfaces than the Inco powder, at least for the powder size and manufacturer recommended machine build parameters that were used in this study. Third, linear patterns can be seen on each surface, although they are not prominent on some surfaces; these correspond to the build layers. Finally, the roughness on the upward-facing and vertical surfaces of the Inco has similar morphology. This is also the case for the CoCr coupons. The roughness of the downward-facing surface appears much different than the other faces.

A detailed examination of the roughness features themselves using the SEM micrographs is useful for understanding some of the heat transfer results reported previously for these specimens [2]. Figure 7 shows a few surfaces at a steep angle as to make the underside of the roughness elements somewhat visible. This shows how the elements appearing spherical from a top view (Fig. 6) are connected to the surface. Figure 7(a) shows that many particles on the upward-facing surface of the Inco coupons appear

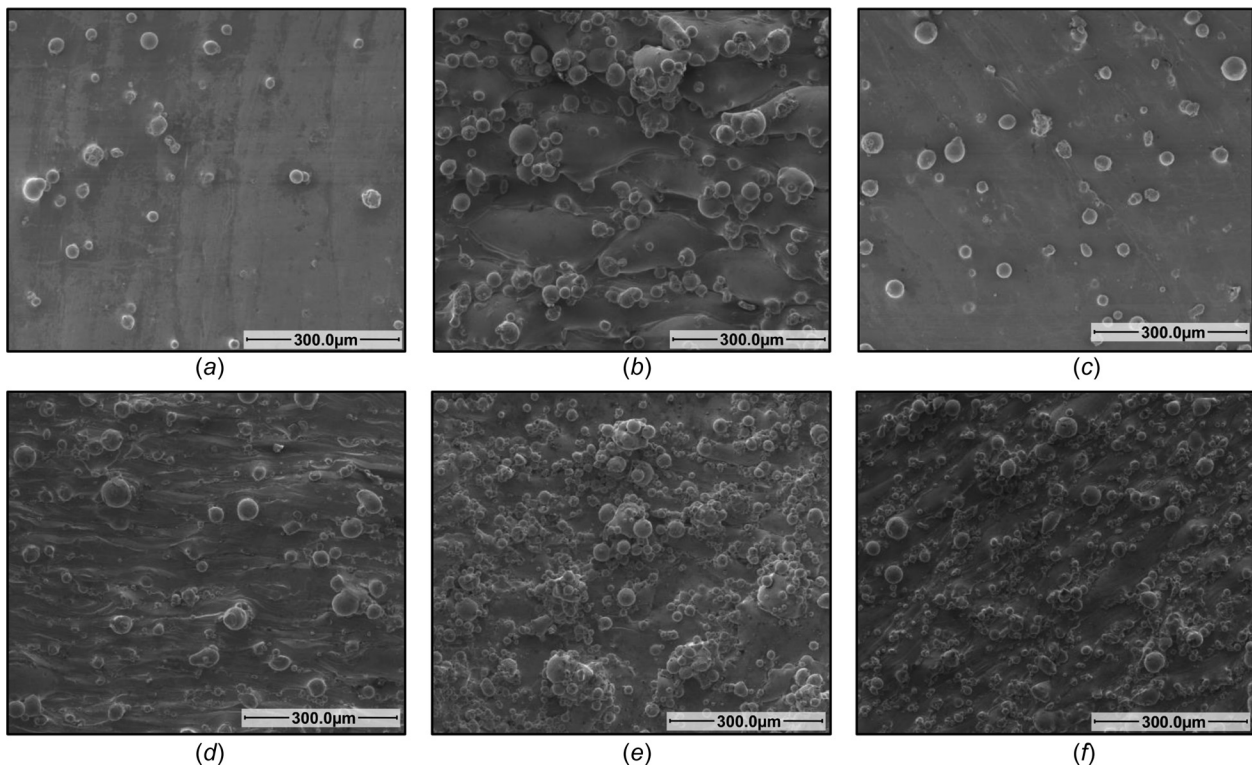


Fig. 6 SEM micrographs of each surface type for both Inco and CoCr coupons: (a) Inco upward-facing, (b) Inco downward-facing, (c) Inco vertical, (d) CoCr upward-facing, (e) CoCr downward-facing, and (f) CoCr vertical

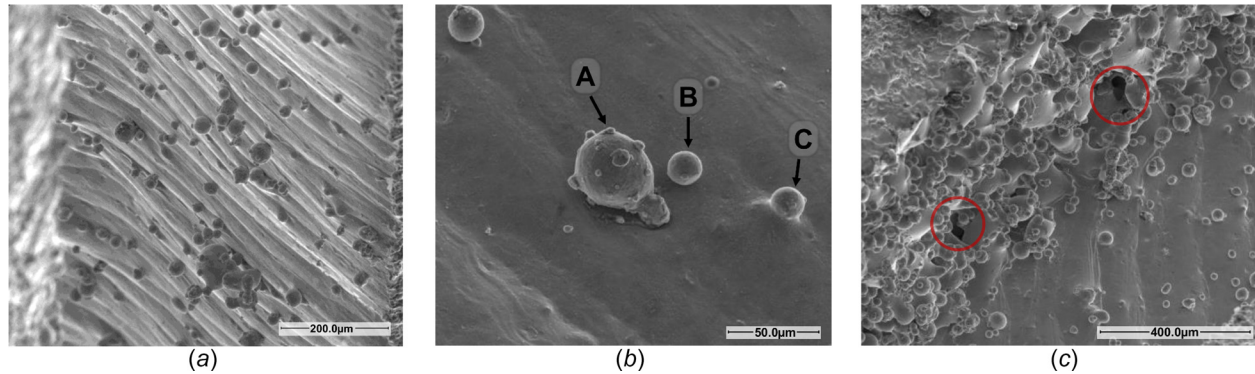


Fig. 7 Angled SEM micrographs of Inco coupon detailing roughness features on vertical and upward-facing surfaces at (a) low magnification and (b) high magnification, and (c) cavities formed on downward-facing surfaces

to be barely connected to the surface. These are particles that sintered to the surface during the building process. Some features appear to be several particles sintered to each other and only a few particles of each group are actually in contact with the surface. This is the nature of all vertically oriented and upward-facing surfaces for both CoCr and Inco coupons although the quantity and size of the features vary between surface orientation and material as shown in Fig. 6.

Figure 7(b) shows details of three particles that illustrate the range of particle adhesion to the surface. Particle A appears to be mostly sintered to the surface and has other particles partially melted or sintered to its surface. Particle B appears to only be partially sintered with minimal contact area. Particle C is fully melted to the surface. A simple Biot number, Bi , calculation can give an approximation of how effective the particles shown in Fig. 7 are at transferring heat. The Biot number definition was derived by taking the ratio of the conductive and convective thermal resistances for the individual particles in Fig. 7(b) using this definition of the Biot number

$$Bi = \frac{R_{\text{cond}}}{R_{\text{conv}}} = \frac{Dh A_{\text{conv}}}{k A_{\text{cond}}} \quad (8)$$

where D is the diameter of the roughness element, h is the convective heat transfer coefficient, k is the thermal conductivity of the metal, A_{conv} is the total wetted surface area of the particle, and A_{cond} is the minimum cross-sectional area at the interface of the surface and the roughness element. Admittedly, this analysis is subjective because the geometric parameters in Eq. (8) can only be estimated from the SEM images. Nonetheless, this serves as an informative order of magnitude estimate.

The Biot number analysis gives estimates of $Bi \approx 0.1$, 1, and 0.01 for particles A, B, and C, respectively. Particle C is a very efficient feature for heat transfer because of the large conduction area and would be beneficial if high heat transfer is desired. On the other hand, particle B is limited in its ability to transfer heat because of the constricted conduction path where it interfaces with the surface. Particles like particle B are not very desirable from a performance perspective as they are less capable of transferring heat to the fluid but have similar friction drag to that of particle C. The thermal performance of particle A is somewhere between the other two particles. Judging from the SEM images shown here, one would expect there to be a broad distribution of Biot numbers among all roughness elements.

The micrograph in Fig. 7(c) shows an interesting topology that cannot be measured with an OP but likely has significant heat transfer implications. Figure 7(c) shows the interface between a vertical surface and downward-facing surface of an Inco coupon. The boundary where the two surfaces intersect extends from the top right to the bottom left corners; the vertical surface is in the

lower right of the image and the downward-facing surface is in the upper left of the image. Two circles indicate areas where cavities in the roughness can be seen. These voids are detrimental to heat transfer and add to the conductive thermal resistance of the roughness.

As stated previously, only the OP data were used to quantify the roughness of the various surfaces. This was done using five different regions of each surface type and material to calculate the average roughness parameters expressed in Eqs. (1)–(5) as well as the correlation length, λ ; the results are plotted in Fig. 8. The statistical uncertainty of these parameters was determined for each surface type and material using the methods described in Ref. [19] with a confidence level of 95%. The number of samples was selected to decrease the statistical uncertainty to a value small enough to expose trends in the data. There is still uncertainty unaccounted for in these values due to a bias that may exist as a result of the data collection or analysis methods. This additional uncertainty is impossible to quantify or even estimate as it would require quantitative knowledge about the surface structure beyond what the OP is capable of giving. The authors believe that a bias error would only contribute a small amount to the overall uncertainty because of the large variation between different samples. Therefore, only the statistical uncertainty is reported.

Figure 8(a) shows that R_a of the CoCr coupons is higher for both the upward-facing and vertical surfaces, which corroborates the observations made from Fig. 6. The downward-facing surfaces have a much greater R_a than the upward-facing and vertical surfaces, and it is nearly identical for both materials even though the morphology observed in Figs. 6(b) and 6(e) is different. R_q shown in Fig. 8(b) shows similar trends to those of R_a . It is difficult to glean much information about R_z from Fig. 8(c) because of the large uncertainty. All that can be said about this parameter is that the downward-facing surface of the Inco coupons has a larger R_z than the others. The skewness shown in Fig. 8(d) is similar for all surfaces except the Inco downward-facing surface. The positive R_{sk} values denote that these surfaces are strongly dominated by positive features, which is corroborated by the SEM images in Fig. 6. The low R_{sk} of the Inco downward-facing surface suggests it has fewer peaks than the other surfaces and reflects the observed difference in morphology between the downward-facing surfaces of the Inco and CoCr coupons. The kurtosis values tell that the distribution width of roughness on all CoCr surfaces is comparable to each other, but the downward-facing Inco surface has a tighter distribution than the other Inco surfaces.

The final parameter, λ , is presented in Fig. 8(f). As stated before, this parameter identifies dominant length scales and periodic patterns. Two major scales can be identified by inspecting the SEM images in Fig. 7. The first is the particle size, which is nominally $30 \mu\text{m}$, and the second is the build layer height which is $40 \mu\text{m}$. Since the coupon was angled at 45 deg while being built,

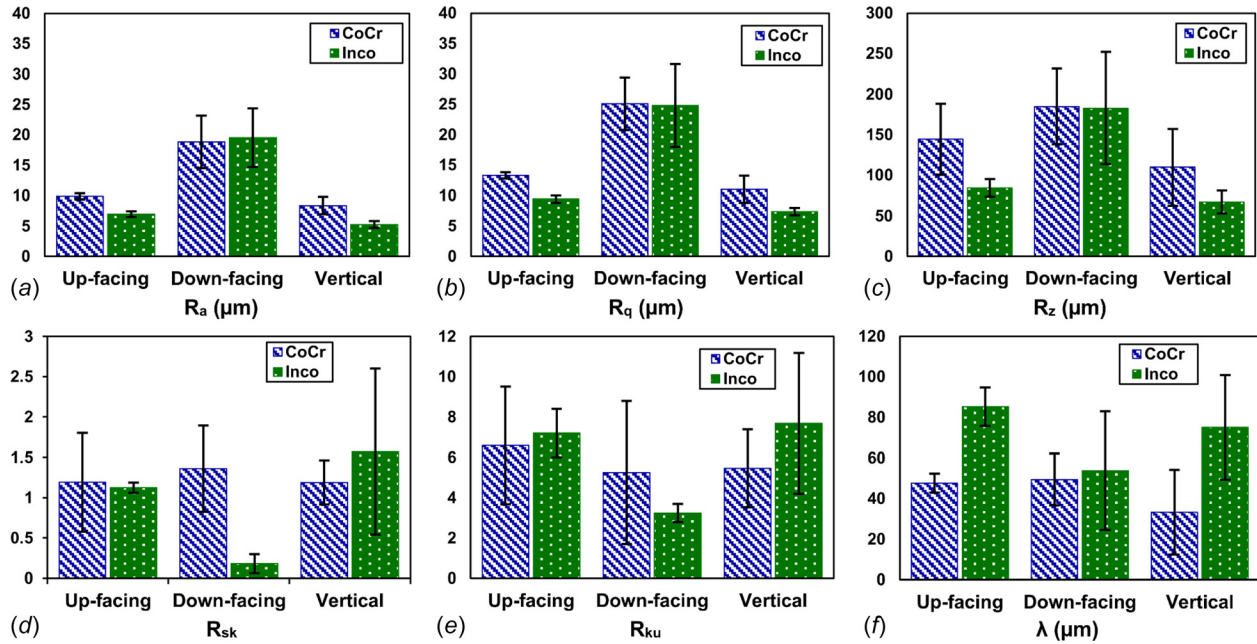


Fig. 8 Averaged roughness parameters with statistical uncertainty of each surface orientation from OP measurements

one would expect that any patterns from the build layers would manifest themselves as $56.6 \mu\text{m}$ ($\sqrt{2} \times 40 \mu\text{m}$) in the flow direction. Judging by the uncertainty magnitudes of λ shown in Fig. 8(f), only three of the six surfaces (CoCr upward-facing, CoCr downward-facing, and Inco upward-facing) appear to clearly have a dominant length scale. The roughness length scale of the CoCr upward-facing and downward-facing surfaces seems to be dominated by the build layer thickness as they are both around $50 \mu\text{m}$. The Inco upward-facing coupon has a higher correlation length of about $85 \mu\text{m}$. The reason for this is unclear, but it is suspected that some layers overlap and create a pattern that is larger than the build layer height. Of the three remaining surfaces, all appear to have different length scales, but their large uncertainty renders observations inconclusive. The correlation length of the vertical CoCr surface appears to be dominated by the particle size length scale while that of the downward-facing Inco surface seems to be strongly influenced by the build layer height. As with the Inco upward-facing surface, the Inco vertical surface has a very long correlation length for which it is unclear why.

Since the flow and heat transfer data reported previously [2] include the combined effect of all surface orientations (i.e., upward-facing, downward-facing, and vertical) and each surface orientation has been shown to differ in roughness from one another, the roughness measurements were combined into an area-weighted average value for each channel for comparison purposes. The areas used for weighting were those measured with the CT scans. The averaged roughness parameters for all coupons are shown in Table 2. One will quickly notice how similar each

parameter is between all coupons of a given material. This is because the aspect ratio of all but the S-2x-Co and S-2x-In is very similar.

All the results shown in Table 2 are consistent with what is observed in the SEM images. R_a , R_q , and R_z are greater for the CoCr coupons albeit only slightly. This is due to the greater roughness on the upward-facing and vertical surfaces of the CoCr coupons. The skewness is also larger with the CoCr coupons, which is primarily due to R_{sk} of the downward-facing surfaces of the CoCr coupons being much greater than that of the downward-facing surfaces of the Inco coupons. The area ratios, A_t/A , A/A_f , and A_f/A_w , are very different between the CoCr and Inco coupons. The reason for this is the greater number of small roughness particles on the CoCr coupon surfaces as shown in Fig. 6. This results in more surface area on the CoCr coupons than the Inco coupons. When these ratios are used to calculate Λ , the resulting difference between the two materials is even more dramatic. However, within each set of coupons of the same material, there is little variation in this parameter.

Heat Transfer and Pressure Loss Correlations. Efforts to correlate the roughness effects just discussed to the equivalent sand grain roughness using approaches found in the literature proved fruitless. Using the same approach taken by van Rij et al. [18], Bogard et al. [20], and Bons [21] was not successful because of the significant difference in Λ between the CoCr and Inco coupons. Because the flow and heat transfer through the coupons of

Table 2 Average coupon roughness parameters measured with an OP

Coupon	R_a (μm)	R_q (μm)	R_z (μm)	R_{sk}	R_{ku}	λ (μm)	A_t/A	A/A_f	A_f/A_w	Λ
L-1x-Co	12.51	16.69	147.84	1.25	5.78	43.84	1.75	2.83	0.424	11.49
L-2x-Co	12.50	16.68	147.76	1.25	5.77	43.82	1.75	2.83	0.424	11.49
M-1x-Co	12.55	16.74	148.14	1.25	5.78	43.93	1.75	2.82	0.425	11.48
M-2x-Co	12.64	16.86	148.98	1.25	5.78	44.16	1.76	2.82	0.425	11.47
S-2x-Co	11.40	15.18	137.68	1.23	5.69	41.01	1.72	2.86	0.422	11.62
L-1x-In	10.83	14.15	113.32	0.93	5.96	71.14	1.27	9.75	0.230	231.9
L-2x-In	10.79	14.11	113.05	0.93	5.97	71.17	1.27	9.75	0.230	231.5
M-1x-In	10.52	13.78	110.81	0.96	6.05	71.35	1.26	9.77	0.227	228.3
M-2x-In	10.63	13.91	111.66	0.95	6.02	71.28	1.27	9.76	0.228	229.5
S-2x-In	9.27	12.26	100.36	1.11	6.44	72.22	1.23	9.82	0.214	213.2

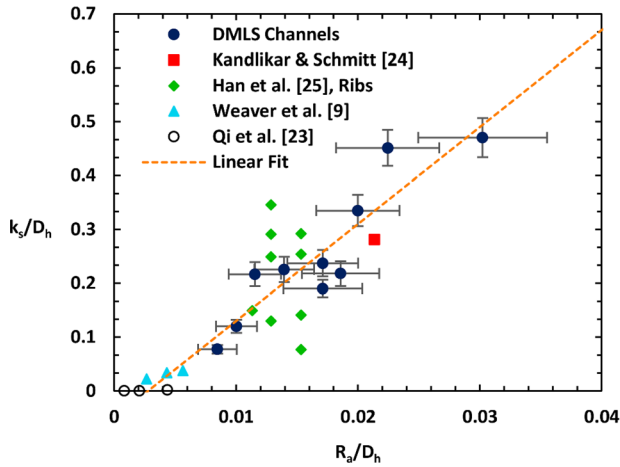


Fig. 9 Relative arithmetic mean roughness, R_a/D_h , plotted versus relative equivalent sand grain roughness, k_s/D_h , for DMLS channels and rough channel data from the literature

the same geometry were not very different between the two materials, Λ was not an effective parameter to correlate with. Other approaches described by Bons [8], Goodhand et al. [16], and Flack and Schultz [22] were also attempted with little or no success. The lack of success likely lies in the fact that these studies were investigating external flows where the boundary layer growth was not constrained by walls.

Surprisingly, one of the simplest statistical measures of channel roughness, R_a/D_h , correlated best with the relative equivalent sand grain roughness, k_s/D_h , in the fully turbulent regime measured previously by the authors [2]. Figure 9 shows these two variables plotted against each other for all DMLS coupons alongside data from the literature which include air flow through rough channels [9], liquid nitrogen flow through rough microchannels [23], air flow through very rough microchannels [24], and air flow through channels with various rib configurations [25]. The DMLS data show error bars that represent the statistical uncertainty of R_a/D_h and the experimental uncertainty of k_s/D_h . A linear fit of the data given by Eq. (9) agrees quite well with the data from the literature except for the ribbed channel data. The reason for this is that the organized roughness of a ribbed channel generates secondary flows that significantly alter the friction. Such secondary flows are not formed by the random roughness of the DMLS channels. The ribbed channel data show that this correlation is best for randomly rough surfaces only

$$\frac{k_s}{D_h} = 18 \frac{R_a}{D_h} - 0.05 \quad (9)$$

Users of this correlation should keep in mind one additional limitation. This correlation is only valid for $R_a/D_h > 0.0028$ as values below this threshold result in a negative k_s/D_h . Relative equivalent sand grain roughness should be assumed to equal zero for $R_a/D_h < 0.0028$. The ability of this new correlation to predict the friction factor was examined by substituting the k_s/D_h predictions of each coupon into Colebrook's equation given in Eq. (10) [26]. These predictions are plotted in Fig. 10 with the data. Although some data are underpredicted and others are overpredicted, there is good agreement for the most part

$$\frac{1}{\sqrt{f}} = -2.0 \log \left(\frac{k_s/D_h}{3.7} + \frac{2.51}{Re\sqrt{f}} \right) \quad (10)$$

As was done with the friction factor data, several approaches were taken in attempt to correlate heat transfer to measured roughness. The first approach examined the total surface area to see if increased surface area is responsible for the augmented heat

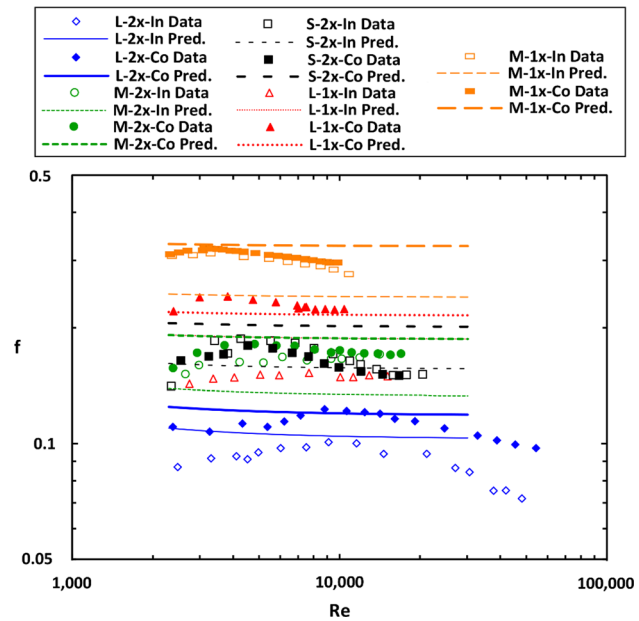


Fig. 10 Friction factor data [2] of DMLS coupons compared to predictions from Eqs. (9) and (10)

transfer. This was unsuccessful because the difference of A_f/A shown in Table 2 is small between the various geometries for a given material and is large between materials. Factors such as Biot number and flow dynamics around the roughness elements are impacting the heat transfer augmentation in addition to the total surface area.

The method that was most successful followed a two-layer model technique used by many [27] which was first introduced by Prandtl [28]. Gnielinski's model [29], given in Eq. (11) in terms of a Nusselt number, Nu , has become one of the most commonly used correlations based on Prandtl's two-layer model and was used here as the basis for developing a correlation. The constants in this new correlation were determined using a fitting algorithm that varied the constants in Gnielinski's correlation while keeping the friction factor and the Prandtl number, Pr , fixed to best match the data. The resulting correlation is given in Eq. (12). Notice that Eq. (12) contains Pr just as the Gnielinski correlation; this was retained for consistency. Because air was the only fluid used in all the experiments, this correlation should only be used to predict heat transfer of fluids where $Pr \approx 0.7$. It should also be noted that this correlation is for turbulent flows only ($Re > 2300$)

$$Nu = \frac{f/8(Re - 1000)Pr}{1 + 12.7\sqrt{f/8}(Pr^{2/3} - 1)} \quad (11)$$

$$Nu = \frac{(Re^{0.5} - 29)Pr\sqrt{f/8}}{0.6(1 - Pr^{2/3})} \quad (12)$$

The accuracy with which Eq. (12) is able to predict the Nu was examined by comparing it to the heat transfer data from the authors' previous paper [2]. For this, two different approaches were taken. The first assumed that no friction information is known a priori, and f in Eq. (12) needed to be estimated. To estimate f , the measured roughness given in Table 2 was used to predict k_s/D_h by means of Eq. (9). This prediction was then used in the Colebrook equation given in Eq. (10) to obtain a prediction of friction factor which was used to predict Nu using Eq. (12). The result of this prediction is shown in Fig. 11 for the Inco coupons and in Fig. 12 for the CoCr coupons. The estimates fall within $\pm 30\%$ of all the data, but many of the predictions are much closer.

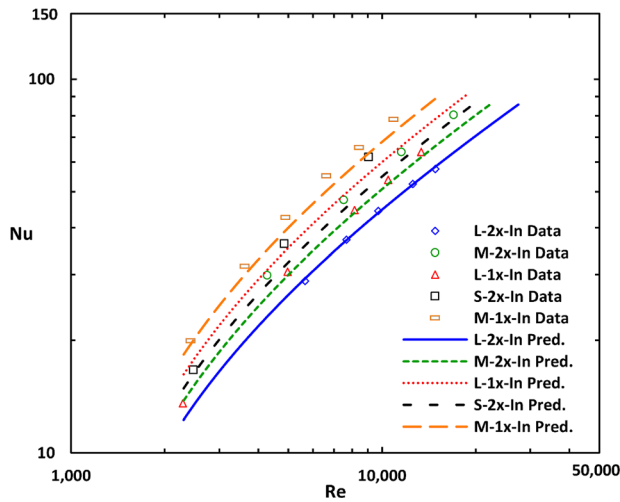


Fig. 11 Nusselt number data [2] of Inco coupons compared to predictions from Eq. (12) where f is calculated using Eqs. (9) and (10)

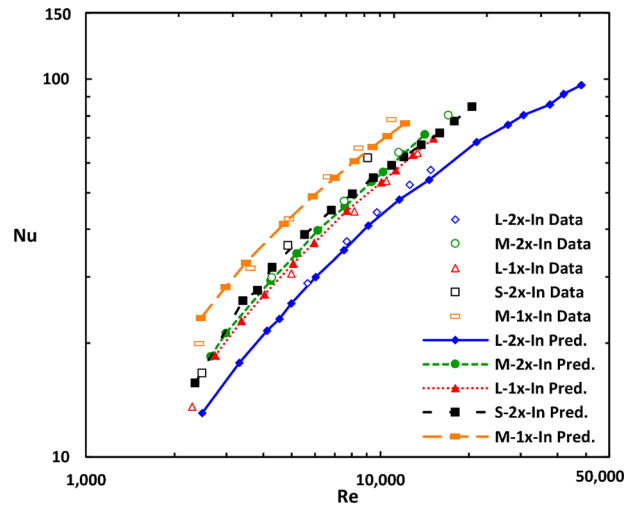


Fig. 13 Nusselt number data [2] of Inco coupons compared to predictions from Eq. (12) where f is from Ref. [2]

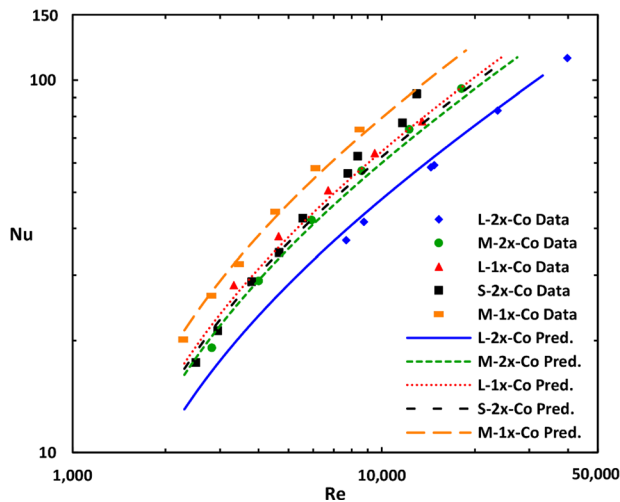


Fig. 12 Nusselt number data [2] of CoCr coupons compared to predictions from Eq. (12) where f is calculated using Eqs. (9) and (10)

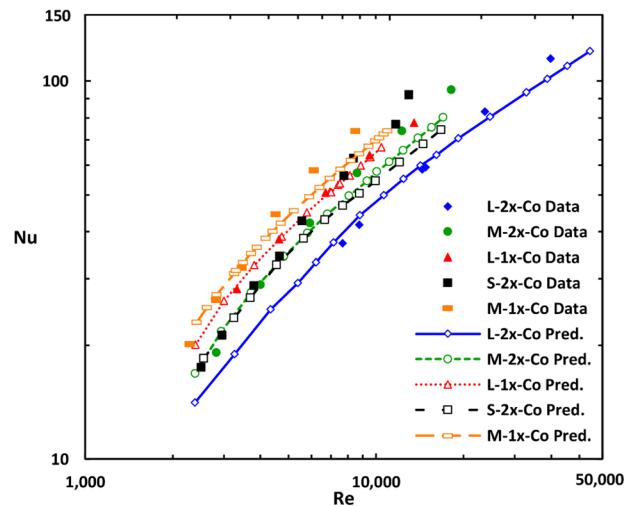


Fig. 14 Nusselt number data [2] of CoCr coupons compared to predictions from Eq. (12) where f is from Ref. [2]

The second approach utilized the friction information to predict Nu. The friction factor data for these coupons were used in Eq. (12) to estimate Nu; a comparison of the prediction and the data is given in Fig. 13 for the Inco coupons and Fig. 14 for the CoCr coupons. This method cuts the variation from $\pm 30\%$ to $\pm 15\%$. However, most of the data are within a few percent of the prediction. This second approach gives better results than the first because there is less uncertainty in the prediction of friction factor in the second approach. Predictions for the data reported by Weaver et al. [9] and Snyder et al. [3] were made using both approaches; these predictions fall within 30% for both methods.

The usefulness of this new correlation is best understood by comparing it to Gnielinski's correlation. Both equations were solved over the range $3000 < Re < 30,000$ and for three different values of k_s/D_h (0.1, 0.2, and 0.4); the Colebrook equation was used in both cases to estimate f from the given k_s/D_h . The estimate of Nu from the Gnielinski correlation is about twice as high as the estimate from Eq. (12) at $Re = 3000$ and about eight times too high at $Re = 30,000$. This new correlation is much more capable of predicting flow for relative roughness between $0.07 < k_s/D_h < 0.5$. Using this correlation outside of this range, particularly at lower values of k_s/D_h , may give erroneous predictions.

These correlations are believed to be generally applicable to internal channels made with laser powder bed fusion from powder that is comparable in size to the work previously reported [2], which describes the characterization of channels made from two different powder types. The fact that comparisons were made using coupons with two different materials whereby the flow friction and heat transfer experiments gave the same results despite strong differences in surface morphology for the two different materials gives credence to the generality of the correlations reported.

Conclusions

AM shows great potential for being used commonly in future gas turbine engines. Understanding the benefits and limitations of processes like DMLS is necessary for designers to properly use this technology. Past studies have shown that the roughness resulting from metal parts made with AM has a strong impact on the flow friction and heat transfer.

This study focused on characterizing the morphology and quantifying the roughness of microchannel surfaces made with DMLS

to develop correlations that relate the physical roughness measurements to the effect the roughness has on the flow friction and heat transfer. Measurements were collected by means of CT scanning, optical profilometry, and scanning electron microscopy. Results from the SEM showed that most roughness elements are powder particles that sinter or partially melt to the surface during the build process. The CoCr coupons appeared to have more particles adhered to the surfaces giving them higher roughness values than the Inco coupons.

Of all the parameters present in the literature used to quantify roughness, the relative arithmetic mean roughness, R_a/D_h , relates best with the relative equivalent sand grain roughness, k_s/D_h . A correlation was presented that correlates R_a/D_h with k_s/D_h for use of estimating the friction factor of flow through a DMLS rough channel. Results of this correlation were in fair agreement with the flow data. A heat transfer correlation is also presented which predicts the Nusselt number of flow through DMLS microchannels using predictions or measurements of friction factor. This new correlation agrees well with the experimental data and significantly improves upon correlations widely used for flow through channels. Results from this paper provide necessary tools for designers that use AM for building parts with small flow channels.

Acknowledgment

The authors would like to thank Pratt & Whitney for the financial and technical assistance throughout this study as well as the staff in the Materials Characterization Laboratory at Penn State who provided necessary equipment and invaluable technical support for this work.

Nomenclature

A = flat area
 A_c = cross-sectional flow area
 A_{cond} = conductive cross section area
 A_{conv} = wetted surface area
 A_f = forward-facing area
 A_t = total surface area
 A_w = windward wetted surface area
ACF = autocorrelation function
Bi = Biot number
 d = diameter of round channel
 D = roughness element diameter
 D_h = hydraulic diameter ($4A_c/p$)
 f = Darcy friction factor
 h = convective heat transfer coefficient
 k = thermal conductivity of coupon
 k_{air} = thermal conductivity of air
 k_s = equivalent sand grain roughness
 n = number of data points
Nu = Nusselt number (hD_h/k_{air})
 p = perimeter
Pr = Prandtl number
 R_a = arithmetic mean roughness
 R_{cond} = conductive thermal resistance
 R_{conv} = convective thermal resistance
 R_{ku} = kurtosis of roughness
 R_q = root-mean-square roughness
 R_{sk} = skewness of roughness
 R_z = mean roughness depth
Re = Reynolds number (VD_h/ν)
 S = channel pitch

V = mass-averaged fluid velocity
 z = roughness height coordinate

Greek Symbols

λ = roughness correlation length
 Λ = roughness density and shape parameter
 μ = mean surface height
 ν = fluid density

References

- [1] GE, 2015, "Additive Manufacturing," General Electric, Fairfield, CT, accessed Oct. 12, 2015, <http://www.ge.com/stories/advanced-manufacturing>
- [2] Stimpson, C. K., Snyder, J. C., Thole, K. A., and Mongillo, D., 2015, "Roughness Effects on Flow and Heat Transfer for Additively Manufactured Channels," *ASME J. Turbomach.*, **138**(5), p. 051008.
- [3] Snyder, J. C., Stimpson, C. K., Thole, K. A., and Mongillo, D., 2016, "Build Direction Effects on Additively Manufactured Channels," *ASME J. Turbomach.*, **138**(5), p. 051006.
- [4] Nikuradse, J., 1933, "Strömungsgesetze in rauhen Röhren," *Forschungsheft 316*, Teil B, Vol. 4, VDI-Verlag, Berlin.
- [5] Moody, L. F., 1944, "Friction Factor for Pipe Flow," *Trans. ASME*, **66**(8), pp. 671–684.
- [6] Schlichting, H., and Klaus, G., 2000, *Boundary Layer Theory*, Springer, New York.
- [7] Schlichting, H., 1936, "Experimentelle Untersuchungen zum Rauheitsproblem," *Ing.-Arch.*, **7**(1), pp. 1–34.
- [8] Bons, J. P., 2010, "A Review of Surface Roughness Effects in Gas Turbines," *ASME J. Turbomach.*, **132**(2), p. 021004.
- [9] Weaver, S. A., Barringer, M. D., and Thole, K. A., 2011, "Microchannels With Manufacturing Roughness Levels," *ASME J. Turbomach.*, **133**(4), p. 041014.
- [10] Huang, K., Wan, J. W., Chen, C. X., Li, Y. Q., Mao, D. F., and Zhang, M. Y., 2013, "Experimental Investigation on Friction Factor in Pipes With Large Roughness," *Exp. Therm. Fluid Sci.*, **50**, pp. 147–153.
- [11] Brackbill, T. P., and Kandlikar, S. G., 2007, "Effects of Low Uniform Relative Roughness on Single-Phase Friction Factors in Microchannels and Minichannels," *ASME Paper No. ICNMM2007-30031*.
- [12] Morini, G. L., 2004, "Single-Phase Convective Heat Transfer in Microchannels: A Review of Experimental Results," *Int. J. Therm. Sci.*, **43**(7), pp. 631–651.
- [13] EOS GmbH, 2011, "Material Data Sheet: EOS CobaltChrome MP1," EOS GmbH, München, Germany.
- [14] EOS GmbH, 2014, "Material Data Sheet: EOS NickelAlloy IN718," EOS GmbH, München, Germany.
- [15] EOS GmbH, 2011, "Basic Training EOSINT M 280," EOS GmbH, München, Germany.
- [16] Goodhand, M. N., Walton, K., Blunt, L., Lung, H. W., Miller, R. J., and Marsden, R., 2016, "The Limitations of ' R_a ' to Describe Surface Roughness," *ASME J. Turbomach.*, **138**(10), p. 101003.
- [17] Dirling, R. B., 1973, "A Method for Computing Roughwall Heat Transfer Rates on Reentry Nosedtips," *AIAA Paper No. 73-763*.
- [18] van Rij, J. A., Belnap, B. J., and Ligrani, P. M., 2002, "Analysis and Experiments on Three-Dimensional, Irregular Surface Roughness," *ASME J. Fluids Eng.*, **124**(3), pp. 671–677.
- [19] Figliola, R. S., and Beasley, D. E., 2005, *Theory and Design for Mechanical Measurements*, Wiley, Hoboken, NJ.
- [20] Bogard, D. G., Schmidt, D. L., and Tabbita, M., 1998, "Characterization and Laboratory Simulation of Turbine Airfoil Surface Roughness and Associated Heat Transfer," *ASME J. Turbomach.*, **120**(2), pp. 337–342.
- [21] Bons, J. P., 2002, "St and cf Augmentation for Real Turbine Roughness With Elevated Freestream Turbulence," *ASME J. Turbomach.*, **124**(4), pp. 632–644.
- [22] Flack, K. A., and Schultz, M. P., 2010, "Review of Hydraulic Roughness Scales in the Fully Rough Regime," *ASME J. Fluids Eng.*, **132**(4), p. 041203.
- [23] Qi, S. L., Zhang, P., Wang, R. Z., and Xu, L. X., 2007, "Single-Phase Pressure Drop and Heat Transfer Characteristics of Turbulent Liquid Nitrogen Flow in Micro-Tubes," *Int. J. Heat Mass Transfer*, **50**(9–10), pp. 1993–2001.
- [24] Kandlikar, S. G., Schmitt, D., Carrano, A. L., and Taylor, J. B., 2005, "Characterization of Surface Roughness Effects on Pressure Drop in Single-Phase Flow in Minichannels," *Phys. Fluids*, **17**(10), p. 100606.
- [25] Han, J. C., Zhang, Y. M., and Lee, C. P., 1991, "Augmented Heat Transfer in Square Channels With Parallel, Crossed, and V-Shaped Angled Ribs," *ASME J. Heat Transfer*, **113**(3), pp. 590–596.
- [26] Colebrook, C. F., 1939, "Turbulent Flow in Pipes, With Particular Reference to the Transition Region Between the Smooth and Rough Pipe Laws," *J. Inst. Civ. Eng.*, **11**(4), pp. 133–156.
- [27] Bhatti, M. S., and Shah, R. K., 1987, "Turbulent and Transition Flow Convective Heat Transfer in Ducts," *Handbook of Single-Phase Convective Heat Transfer*, Wiley, New York.
- [28] Prandtl, L., 1910, "Eine Beziehung zwischen Wärmeaustausch und Strömungswiderstand der Flüssigkeiten," *Z. Für Phys.*, **11**, pp. 1072–1078.
- [29] Gnielinski, V., 1976, "New Equations for Heat and Mass Transfer in Turbulent Pipe and Channel Flow," *Int. Chem. Eng.*, **16**(2), pp. 359–368.